INTERNATIONAL JOURNAL FOR NUMERICAL METHODS IN FLUIDS, VOL. 14, 1261–1287 (1992)

A FINITE DIFFERENCE METHOD FOR 3D FLOWS ABOUT BODIES OF COMPLEX GEOMETRY IN RECTANGULAR CO-ORDINATE SYSTEMS

HIDEAKI MIYATA AND YOSHIHIRO YAMADA

Department of Naval Architecture and Ocean Engineering, University of Tokyo, Hongo, Bunkyo-ku, Tokyo 113, Japan

SUMMARY

A finite difference simulation method is developed for 3D flow about a body of complex geometry. The Navier–Stokes equation is approximated by a high-order-accurate difference scheme in the framework of rectangular co-ordinate systems. The configuration of the 3D body is represented by use of both surface porosity and volume porosity and the no-slip body boundary conditions are approximately implemented on the boundary cells. The validity of the method is demonstrated by a numerical test of flow past a sphere at a Reynolds number of 1000. The complicated structure of separated vortices is well revealed by this test computation. The versatility of the method is shown by application to an ocean-engineering problem of flow about a bay with an island.

KEY WORDS Finite difference method Separating flow Ocean current Vortex Zoning method

1. INTRODUCTION

Computational fluid dynamics has made remarkable progress during the last decade because a number of researchers have devoted a great deal of effort to the subject and computer technology has made rapid advances. Current efforts are being focused on applications of computational fluid dynamics to a variety of research problems which are important from either the scientific or engineering viewpoint.

One of the important problems in engineering science is that of drag forces on a body moving at a steady speed or standing still in a uniform stream. The most important component of drag is caused by the separating flow, which is called pressure drag or drag due to vortex generation. In order to design a body configuration of minimum drag, elucidation of the structure of separating flow and the mechanism of vortex shedding is most important. Reduction of drag can be achieved only when the flow is fully understood. A sound understanding of the physical phenomenon that connects the body configuration with the related forces often gives a breakthrough in the design of minimum drag configuration. One example is the relation between ship hull configuration and wave resistance. After the non-linear wave-making phenomenon called the free surface shock wave had been elucidated by experiment,[1] a finite difference method was developed for simulation of non-linear ship waves.[2] The successful application of numerical methods to the Euler equation in engineering is also observed in the field of aeronautics. In the field of ocean engineering there are a variety of fluid dynamical problems in which 3D non-linear fluid motions and resultant forces are important. A numerical simulation method which can cope with these problems and is convenient to use would certainly contribute to the progress of ocean engineering.

0271-2091/92/111261-27$13.50

Received February 1991
Revised August 1991

Finite difference methods employing the boundary-fitted curvilinear co-ordinate system have been developed and promising simulation results have been obtained for viscous flow problems. These will undoubtedly make an important contribution to the elucidation of the structure of viscous separating flows as well as the mechanism of 3D vortex shedding. However, there are many cases in which the configuration of a body is too complex for the boundary-fitted co-ordinate system or the effort of grid generation is tremendous, and these methods are not suitable for practical engineering purposes at present.

For some engineering and scientific problems the use of rectangular co-ordinate systems may be worth consideration. The advantages of inflexible rectangular co-ordinate systems can surpass the inherent disadvantages, since they are able to cope with boundaries of complex geometry with extremely small effort of grid generation. Flow about a body of extremely complicated geometry and flow within complicated boundary configurations can be dealt with by these co-ordinate systems. One example is the flow problem in ocean engineering. The geometry is often so complicated with islands and seamounts that the use of boundary-fitted co-ordinate systems is not practicable. A more practicable method must be developed by approximately implementing the viscous motions on the boundaries of the complicated geometry.

A number of finite difference simulation methods have been developed in the framework of inflexible rectangular grid systems. The MAC method[3] and its improved versions such as the SOLA method[4] have been applied in many research fields. However, the boundary conditions on the body boundary and on the free surface were treated very grossly. A new technique has been devised to implement the free-slip body boundary condition on the hull surface of a ship in the TUMMAC-IV method.[5] Since no effort is required for grid generation and consequently the simulated wave system can be obtained in a reasonable time of execution by a workstation with sufficient degree of accuracy, this method is convenient to use in practice.

In this study the no-slip body boundary conditions are approximately implemented on the boundary cells about a 3D geometry of arbitrary configuration in the rectangular co-ordinate system. The usefulness of this method is examined by simulation of flow past a sphere and it is applied to an ocean-engineering problem with complex geometry. The overall computational procedure is described in Section 2 and details of the treatments to implement the body boundary conditions are described in Section 3. The zoning method is described in Section 4. Simulation of flow past a sphere is described in Section 5. Simulation of flow in Sagami Bay is presented in Section 6 with computer graphic drawings. Brief concluding remarks are given in Section 7.

2. COMPUTATIONAL PROCEDURE

2.1. Grid system

In order to avoid the difficulties of generating boundary-fitted curvilinear grid systems, inflexible rectangular grid systems are employed here. The advantages of choosing this grid system are that elaborate efforts to generate a 3D curvilinear grid system with proper clustering, smoothing and normalizing are not necessary and that it can cope with bodies of extremely complex geometry. It is imagined that generation of a curvilinear grid system is difficult for an oil-drilling platform which is composed of a number of member structures and floating on a rough sea with breaking waves. The boundary-fitted grid system encounters serious difficulties in fitting to boundaries of complicated geometry in ocean-engineering problems.

The most serious disadvantage of the rectangular grid system is that the complicated viscous flow in the boundary layer is very grossly simulated owing to the coarse grid spacing and the approximations introduced in the calculations near the body boundaries. Another disadvantage

is that some ingenious treatments must be devised so that calculations in the boundary cells, where the body surface of complex geometry intersects the underlying grid lines in a variety of ways, do not diverge by not satisfying the conservation properties.

Therefore it is safe to say that the choice of the rectangular grid system restricts the problems to which the method can be applied. For instance, it cannot be used for simulation of a viscous boundary layer on a ship surface beneath the free surface. However, it may be useful for simulation of flow in a bay with islands.

A staggered grid system is employed and the pressure and velocities are defined at the centre of a cell and at the centres of cell surfaces respectively as shown in Figure 1.

2.2. *Governing equations*

The governing equations are the continuity equation and the Navier–Stokes equation as follows. The laws of mass conservation and momentum conservation are implemented by proper solution of these equations. The gradient form is employed for the convective terms for simplicity in approximating into difference forms. All variables are made dimensionless with respect to the uniform flow velocity, the length of the body and the time required for the uniform flow to travel the length of the body. The stagnant pressure is assumed to be 0·5.

$$\nabla \cdot \mathbf{u} = 0, \tag{1}$$

$$\frac{\partial}{\partial t}\mathbf{u} = -\nabla P + \mathbf{a}, \tag{2}$$

$$\mathbf{a} = -(\mathbf{u}\cdot\nabla)\mathbf{u} + (Re^{-1} + v_s)\nabla\cdot\nabla\mathbf{u} + (\nabla v_s)\mathbf{S} + \mathbf{M} + \mathbf{F}, \tag{3}$$

where

$$\mathbf{u} = (u, v, w), \qquad \nabla = \left(\frac{\partial}{\partial x}, \frac{\partial}{\partial y}, \frac{\partial}{\partial z}\right),$$

$$\mathbf{a} = (a_x, a_y, a_z), \qquad \mathbf{M} = (M_x, M_y, M_z), \qquad \mathbf{F} = (F_x, F_y, F_z), \tag{4}$$

$$\mathbf{S} = \begin{bmatrix} 2\dfrac{\partial u}{\partial x} & \dfrac{\partial u}{\partial y} + \dfrac{\partial v}{\partial x} & \dfrac{\partial u}{\partial z} + \dfrac{\partial w}{\partial x} \\ \dfrac{\partial v}{\partial x} + \dfrac{\partial u}{\partial y} & 2\dfrac{\partial v}{\partial y} & \dfrac{\partial v}{\partial z} + \dfrac{\partial w}{\partial y} \\ \dfrac{\partial w}{\partial x} + \dfrac{\partial u}{\partial z} & \dfrac{\partial w}{\partial y} + \dfrac{\partial v}{\partial z} & 2\dfrac{\partial w}{\partial z} \end{bmatrix}.$$

Here $\mathbf{u}$ is the velocity, P is the pressure, Re is the Reynolds number, v_s is the eddy viscosity coefficient of the subgrid-scale (SGS) turbulence model and $\mathbf{M}$ is the numerical dissipation term, which is explained later. The last term $\mathbf{F}$ is the external force, which is used to accelerate the flow from the rest condition to the steady uniform flow condition in this study. The x-axis is taken parallel to the uniform flow direction, y in the lateral direction and z in the vertical direction.

The SGS turbulence model is introduced in the same way as in previous work.[6] However, it is much simpler since an inflexible grid system is employed in this study. The use of the SGS turbulence model is not wholly appropriate because the grid spacing is too coarse for this model

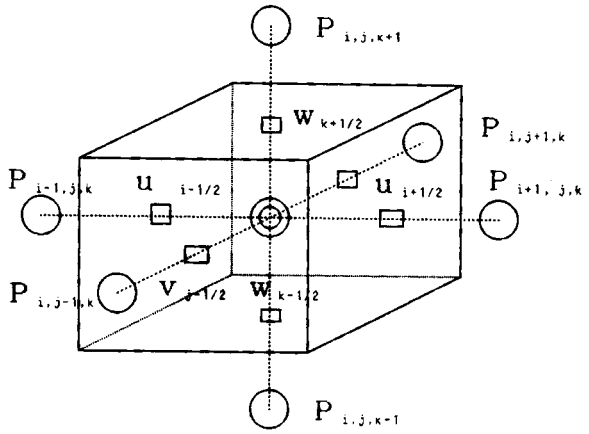

Figure 1. Velocity and pressure points

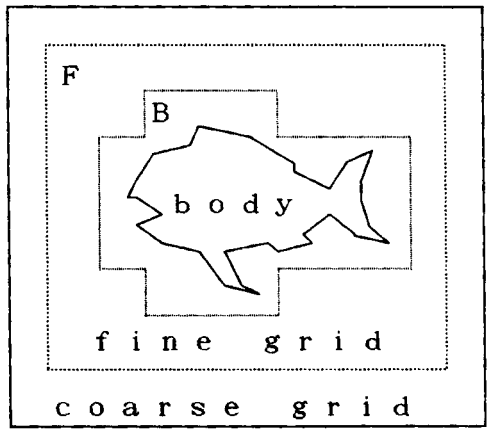

Figure 2. Schematic sketch of zoning

to work properly. Therefore it is only tentatively incorporated here, in anticipation of future extension of this method.

2.3. Zoning

The computational domain is divided into two regions: the inner region including the body and the outer region surrounding the inner region as shown in Figure 2. In order to reduce the total number of cells and to raise the computational efficiency, fine spacing is used in the inner region and relatively coarse spacing in the outer region.

2.4. Algorithm

The computational algorithm is almost the same as in previous work[5] on the simulation of ship waves except for the procedures associated with zoning and the body boundaries.

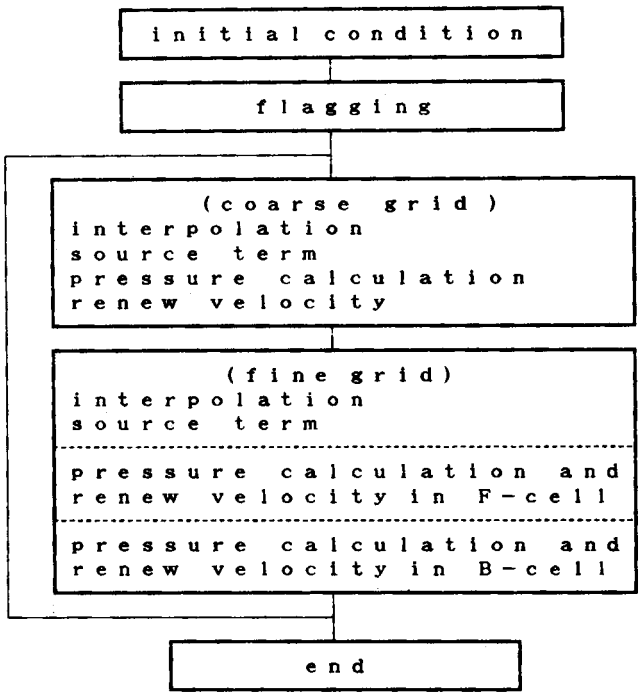

Figure 3. Computational procedure

The computational procedure is illustrated in Figure 3. Firstly flagging is performed so that cells defined as boundary cells successively enclose the body. At each time step in the time-marching procedure, updating of both velocity and pressure fields is first done in the outer region following the algorithm of the MAC method[3] and then done in the inner region making use of the flow variables in the outer region as boundary values. At the next time level the computation in the outer region is repeated with the boundary values in the inner region. The detailed treatments at the interface between two regions are described later.

In the full-of-fluid cells the Poisson equation for the pressure is solved by the Richardson method as

$$\nabla \cdot \nabla P = \nabla \cdot (\mathbf{a} + \mathbf{u}^{(n)}/\Delta t) = \nabla \cdot \mathbf{b}, \tag{5}$$

$$P^{m+1} = P^m + \omega(\nabla \cdot \nabla P - \nabla \cdot \mathbf{b}). \tag{6}$$

Here Δt is the time increment and ω is the relaxation factor set at a value smaller than unity. The superscript n denotes the time level and m the iteration level. In the boundary cells the simultaneous iterative method employed for the fulfilment of the free-slip body boundary conditions in previous work[5] is used:

$$P^{m+1} = P^m + \frac{\omega}{A} D. \tag{7}$$

Here D is the divergence of a cell and A is defined as follows using the volume porosity (γ), which indicates the volume ratio of fluid in the boundary cell:

$$A=\Delta t\left(\frac{\gamma_{i+1}+\gamma_{i-1}}{(\Delta x)^2}+\frac{\gamma_{j+1}+\gamma_{j-1}}{(\Delta y)^2}+\frac{\gamma_{k+1}+\gamma_{k-1}}{(\Delta z)^2}\right), \tag{8}$$

where Δx, Δy and Δz are grid spacings.

The velocity field is updated at each time level as

$$\mathbf{u}^{(n+1)}=\mathbf{u}^{(n)}+\Delta t(-\nabla P+\mathbf{a}). \tag{9}$$

2.5. *Differencing scheme*

For the first derivative of velocity, fourth-order centred differencing is used. For the term $\partial u/\partial x$ at $i+\frac{1}{2}$, for example, it is written as

$$\frac{-u_{i+5/2}+8u_{i+3/2}-8u_{i-1/2}+u_{i-3/2}}{12\Delta x}. \tag{10}$$

Here the subscripts j and k are dropped for simplicity. This scheme is sufficiently accurate and the truncation error is of the form of the fifth derivative of velocity. However, it may be liable to cause nstability of the solution. Therefore the following numerical dissipation of the form of the fourth lerivative of velocity is introduced:

$$\begin{aligned}
M_x&=-\frac{\alpha_4}{24}\left(|u|\Delta x^3\frac{\partial^4}{\partial^4 x}+|v|\Delta y^3\frac{\partial^4}{\partial^4 y}+|w|\Delta z^3\frac{\partial^4}{\partial^4 z}\right)u,\\
M_y&=-\frac{\alpha_4}{24}\left(|u|\Delta x^3\frac{\partial^4}{\partial^4 x}+|v|\Delta y^3\frac{\partial^4}{\partial^4 y}+|w|\Delta z^3\frac{\partial^4}{\partial^4 z}\right)v,\\
M_z&=-\frac{\alpha_4}{24}\left(|u|\Delta x^3\frac{\partial^4}{\partial^4 x}+|v|\Delta y^3\frac{\partial^4}{\partial^4 y}+|w|\Delta z^3\frac{\partial^4}{\partial^4 z}\right)w.
\end{aligned} \tag{11}$$

The parameter α_4 is controlled to be as small as possible so that it does not contaminate the solution. When the Reynolds number is small and the spacing is sufficiently small, α_4 can be set at the value 0·5 as in previous work on wall boundary layers.[7] In this study, in which relatively large spacing is used, it is set at 6·0.

For both the second derivatives in the diffusion term of equation (3) and the second derivatives in the Poisson equation (5), second-order centred differencing is used. In the vicinity of the boundaries, where a sufficient number of velocity points are not available, a lower-order differencing scheme must be introduced as will be described later. For the time differencing, forward differencing is used, except for the convective terms for which the Adams–Bashforth method is employed.

3. BODY BOUNDARY CONDITIONS

3.1. *Porosity*

Since the body surface of complex geometry intersects the underlying grid lines in a variety of ways, the use of segments, which were employed in the 2D case,[8] makes the method extremely complicated. Therefore the body configuration is approximately represented by the volume

porosity and the surface porosity. The volume porosity (γ) is the proportion of fluid in a cell and the surface porosity (β) is the proportion of the cell surface which is not occupied by the body. The latter is similar to the so-called 'window' through which fluid can move, which was introduced in the simulation method for ship waves.[5]

As listed in Table I, the volume porosity is defined at the centre of a cell (pressure point) and is used for flagging of cells, for the choice of differencing scheme, for approximate estimation of the distance to the body surface and for solution of the Poisson equation of pressure in the vicinity of the body surface by equations (7) and (8). The surface porosity is defined at the velocity point and is used for calculation of the divergence of a cell, for the choice of differencing scheme and for approximate estimation of the distance to the body surface. The definition of the surface porosity is illustrated in Figure 4 in a 2D manner. The surface porosity is estimated as the mean of the volume porosities of two cells which are connected by the cell surface where it is defined.

3.2. Flagging

All cells are flagged according to the value of the volume porosity as shown in Table II. Since the pressure point is located at the centre of a cell, it is inside the body when the value of the

Table I. Definition and usage of porosity

	Volume porosity	Surface porosity
Symbol	γ	β
Definition	Ratio of fluid volume in one cell	$\frac{\gamma^i + \gamma^{i+1}}{2}$
Definition point	Pressure point	Velocity point
Usage	Flagging, choice of difference scheme	Choice of difference scheme, divergence calculation, representation of body configuration

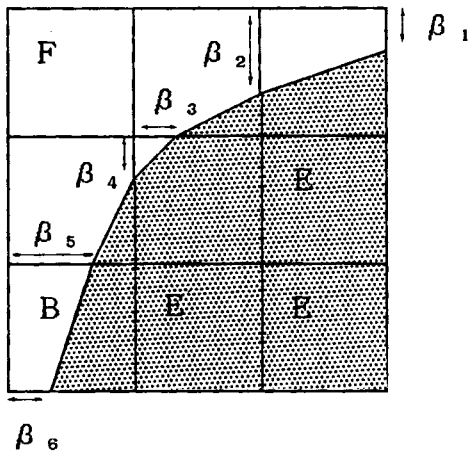

Figure 4. Definition of body configuration by surface porosity

Table II. Volume porosity and method of pressure computation

Volume porosity	Flag	Pressure calculation
$\gamma = 1{\cdot}0$	F	Richardson method
$0{\cdot}5 \leqslant \gamma \leqslant 1{\cdot}0$	B, B*	Simultaneous iterative method
$\gamma < 0{\cdot}5$	E	None

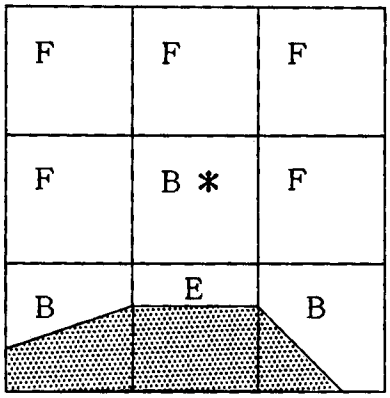

Figure 5. Cell flagging

Table III. Surface porosity and method of updating velocity

Surface porosity	Cell combination	Velocity calculation
$\beta = 1{\cdot}0$	B*–B*, B*–B B–F	N–S equation
$0{\cdot}5 \leqslant \beta < 1{\cdot}0$	B*–B, B–E	Extrapolation
$\beta < 0{\cdot}5$	B*–E, B–E E–E	None

volume porosity is less than 0·5. Therefore a cell whose volume porosity is less than 0·5 is defined as an empty (E) cell and the pressure is not calculated in this cell. A boundary (B) cell is defined as a cell whose volume porosity is greater than 0·5 and less than 1·0. In order to continuously distribute boundary cells along the body surface, some full-of-fluid (F) cells are additionally flagged as special boundary (B*) cells as illustrated in Figure 5.

As described in Table II, the method of pressure computation depends on the flagging. Therefore the pressure computation in boundary cells is performed separately from the computation in F-cells.

After the pressure field has been updated, the velocity field is successively updated by use of the momentum equation at each time level. However, as listed in Table III, the velocity is determined by extrapolating from outside on the cell surfaces whose surface porosity is less than 1·0 and greater than 0·5. This is because updating the velocity by the momentum equation gives

erroneous values for the velocities in the close vicinity of the body surface where the no-slip body boundary conditions must be taken into account. The velocity is extrapolated from each direction by the second-order parabolic curve with its axis parallel to the grid line as shown in Figure 6 and the following averaging operation is done so that the extrapolation is performed in the direction approximately normal to the body surface:

$$u=\sqrt{\left(\frac{\beta-0{\cdot}5}{\beta+0{\cdot}5}\right)}\frac{\beta_{i+1}u_{i+1}+\beta_{i-1}u_{i-1}+\beta_{j+1}u_{j+1}+\beta_{j-1}u_{j-1}+\beta_{k+1}u_{k+1}+\beta_{k-1}u_{k-1}}{\beta_{i+1}+\beta_{i-1}+\beta_{j+1}+\beta_{j-1}+\beta_{k+1}+\beta_{k-1}}. \quad (12)$$

Here u and β are assumed to be defined at (i, j, k) and the subscripts i, j and k are dropped unless they have other values by shifting by ± 1. The value of β is set at zero when it is less than 0·5, because the velocity is not defined in this case as shown in Table III.

3.3. Differencing scheme near the body boundary

In the vicinity of the body boundary the normal five- or three-point centred differencing method cannot be applied owing to the lack of available velocity points. Therefore a lower-order-accurate differencing scheme is inevitably introduced here. For the choice of lower-order-accurate differencing scheme, flagging is done as shown in Table IV and Figure 7. The first and second derivatives of velocity as well as the artificial dissipation term are evaluated at the points marked by circles, while the number of available velocity points, marked by squares, varies depending on

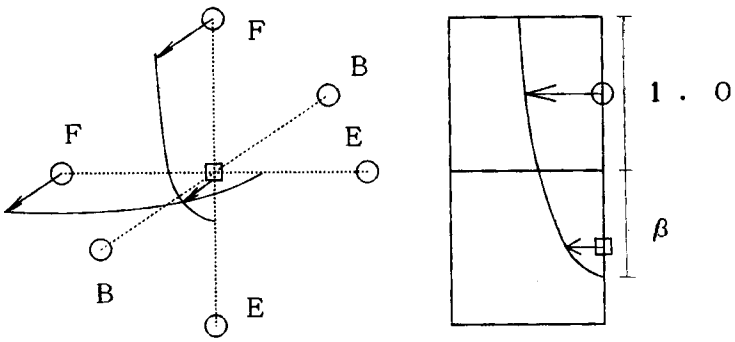

Figure 6. Velocity extrapolation in vicinity of body surface

Table IV. Flagging for choice of difference scheme

Derivative	Flag	Number of available velocity points	No-slip condition
$\partial_x u$, $\partial_y v$, $\partial_z w$	n1	5	—
	n2	3	—
	n3	2	Included
$\partial_x v$, $\partial_x w$, $\partial_y w$, $\partial_y u$, $\partial_z u$, $\partial_z v$	t1	5	—
	t2	3	—
	t3	2	Included
	t4	2	Included

the cases in Figure 7. The cases flagged n1 and t1 are those for which the normal differencing scheme previously described in Section 2.5 is applied.

The choice of differencing scheme, which depends on the flag, is listed in Tables V–VII for the first and second derivatives and the numerical dissipation term respectively. Here Δ is the spacing and I is the shift operator defined as

$$I^m f(x)=f(x+m\Delta x). \tag{13}$$

The no-slip condition is incorporated in these schemes and the distance from the velocity point to the body surface is approximately evaluated by the volume porosity for the case n3 and by the

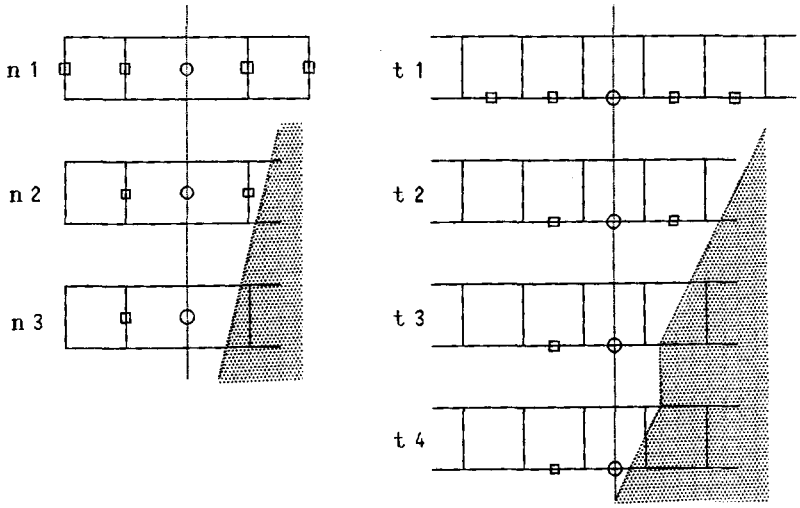

Figure 7. Flagging for choice of difference scheme

Table V. Difference scheme for first derivative

Flag	
n1, t1	$\dfrac{-I^2+8I-8I^{-1}+I^{-2}}{12\Delta}$
n2, t2	$\dfrac{I-I^{-1}}{\Delta}$
n3	$\dfrac{\gamma^2 I+(1-\gamma^2)I^0}{\gamma(1+\gamma)\Delta}$
t3 ($h=\beta+0{\cdot}5$)	$\dfrac{h^2 I+(1-h^2)I^0}{h(1+h)\Delta}$
t4 ($h=\beta-0{\cdot}5$)	$\dfrac{h^2 I+(1-h^2)I^0}{h(1+h)\Delta}$

Table VI. Difference scheme for second derivative

Flag	
n1, n2, t1, t2	$\dfrac{I - 2I^0 + I^{-1}}{\Delta^2}$
n3	$\dfrac{2\gamma I - 2(1+\gamma)I^0}{\gamma(1 \pm \gamma)\Delta^2}$
t3 ($h = \beta + 0{\cdot}5$)	$\dfrac{2hI - 2(1+h)I^0}{h(1+h)\Delta^2}$
t4 ($h = \beta - 0{\cdot}5$)	$\dfrac{2hI - 2(1+h)I^0}{h(1+h)\Delta^2}$

Table VII. Difference scheme for artificial dissipation term

Flag	
n1, t1	$\dfrac{I^2 - 4I + 6I^0 - 4I^{-1} + I^2}{\Delta^4}$
n2, t2	$\dfrac{I - 2I^0 + I^{-1}}{\Delta^2}$
n3, t3, t4	0

surface porosity for the cases t3 and t4. In the vicinity of the body boundary, three-point centred differencing with equal or unequal spacing is employed. It is noted that the first-order numerical dissipation of the second-derivative form is inevitably introduced instead of the third-order numerical dissipation of the fourth-derivative form when the flag is n2 or t2.

4. ZONING

4.1. Zone division

In order to raise the economical efficiency, a zoning technique is incorporated in this simulation method. It is safe to allot relatively coarser grid spacing in the region where the physical phenomena do not involve small-scale motions or do not render significant influences. Since the present method is mostly designed for open boundary problems, e.g. flow about a moving body, the region with coarser spacing may be located outside the inner region with finer spacing so that the detailed flow mechanism may be resolved by the sufficiently fine spacing in the vicinity of the body.

In this study the spacing in the x-direction (Δx) is set the same for both the fine and coarse regions, but the other two spacings (Δy and Δz) in the coarse region are set at double the finer spacings as shown in Table VIII.

Table VIII. Grid spacing

Fine grid	Coarse grid
$\Delta x = \Delta y = \Delta z = \Delta$	$2\Delta x = \Delta y = \Delta z = 2\Delta$

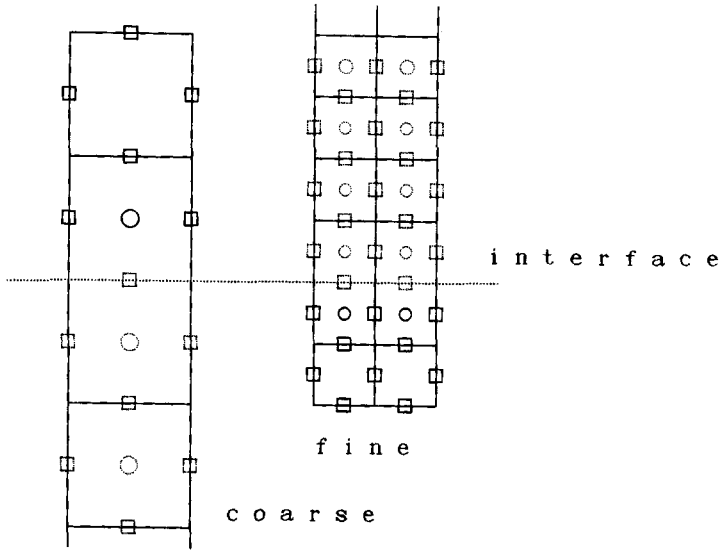

Figure 8. Velocity and pressure points at interface

4.2. Interfacing

The outer region with the coarse grid system and the inner region with the fine grid system have an overlapped part as shown in Figure 8, in which rectangles indicate velocity points and circles pressure points. Only the pressure inside the interface is normally calculated and the pressure marked by a solid circle is set at the boundary value. The velocities marked by solid rectangles in the overlapped region are necessary for the evaluation of the source term of the Poissson equation for the pressure, since the five-point differencing scheme is employed for both the convective and artificial dissipation terms.

The pressure and velocities in the overlapped region are determined by interpolating the values of the other region. When the computation in the coarser grid region is finished, the values in the overlapped part of the finer grid region are updated by linearly interpolating the values in the overlapped part of the coarser grid region, which is just updated by the following equations for the case illustrated in Figure 9, in which P_a is to be computed in the finer grid region:

$$P_b = (P_1 + 3P_2 + 3P_3 + 9P_4)/16, \tag{14}$$

$$V_a = (V_1 + V_2 + 3V_3 + 3V_4)/8, \tag{15}$$

$$V_b = (V_2 + 3V_4)/4, \tag{16}$$

These values are used as boundary values for the computation in the finer grid system. When the computation in the finer grid region is finished and the time level is advanced, the values in the

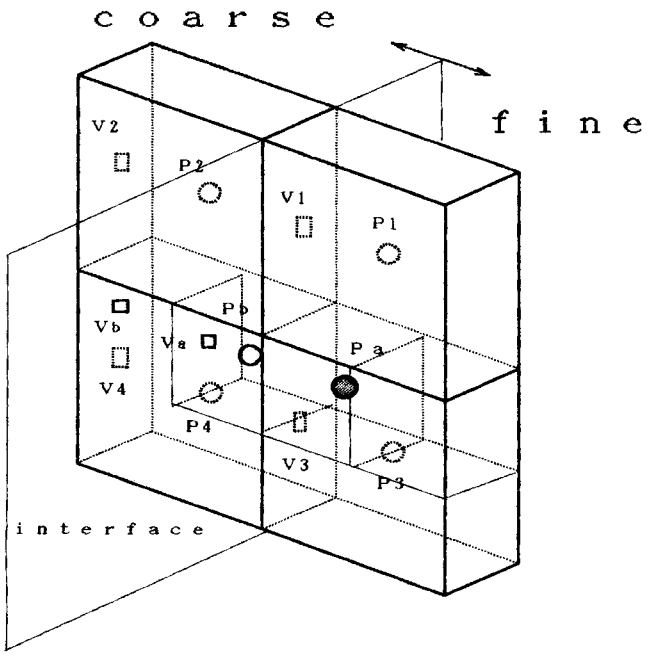

Figure 9. Definition sketch for interpolation from coarse to fine grids

overlapped part of the coarse grid region are set by linearly interpolating the values in the overlapped part of the finer grid region.

In the case illustrated in Figure 10 the following interpolation procedures are performed for the computation of the pressure P_A in the coarser grid region:

$$P_B=(P_1+P_2+P_3+P_4)/4, \tag{17}$$

$$V_A=(V_1+V_2)/2, \tag{18}$$

$$V_B=(V_3+V_4)/2. \tag{19}$$

The use of linear equations for the interpolation is supposed to be favourable for the conservation of mass and momentum at the interface as discussed by Rai.[9]

5. FLOW PAST A SPHERE

5.1. Conditions of computation

The flow past a sphere is chosen as an example to demonstrate the overall appropriateness of the present method and to examine its degree of accuracy. Although this flow is one of the most typical, the structure of the flow behind a sphere is not yet well understood, notwithstanding the work by Taneda,[10] Achenbach[11] and others. Therefore simulation of this flow is interesting from the scientific point of view.

The computational domain is shown in Figure 11. The inner region of cross-section 2·0 × 2·0 is made of finer grids and the outer region of coarser grids. A three-grid test is performed under the

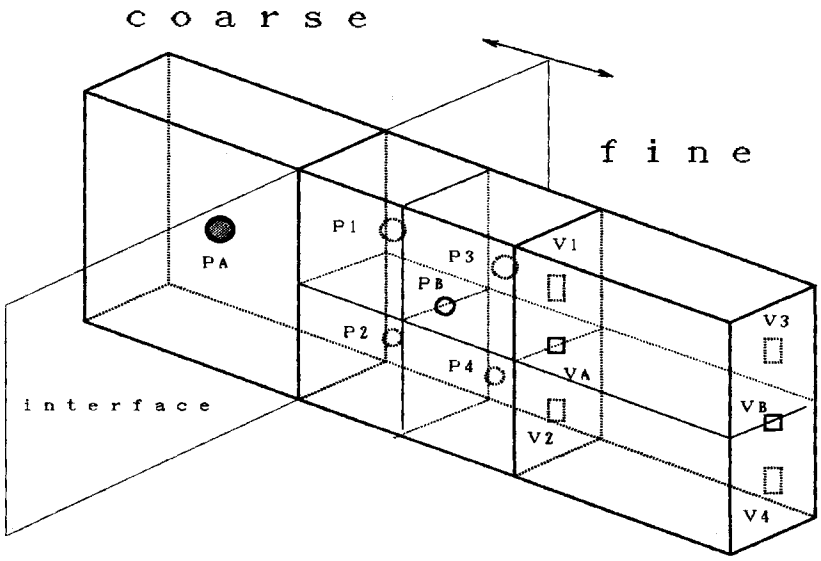

Figure 10. Definition sketch for interpolation from fine to coarse grids

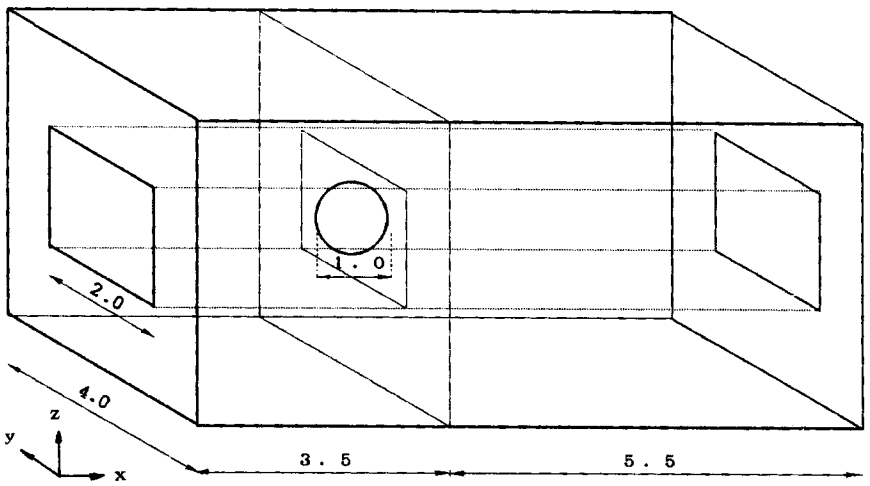

Figure 11. Computational domain

conditions listed in Table IX. The diameter of the sphere is divided into 12, 16 and 20 cells in the cases (a), (b) and (c) respectively. The Reynolds number based on the diameter of the sphere and the uniform flow velocity is set at 1000. The time increment is varied depending on the grid spacing so that the Courant number is invariant throughout the three cases.

The computation was executed on a TITAN-II graphic supercomputer and the required CPU time was shown in Table IX. For case (b) with an elongated computational domain the computation was continued until the non-dimensional time reached 30, while it was stopped at $T=20$ for the other cases.

Table IX. Conditions of computation

	(a)	(b)	(c)
Cell size Δ	1/12	1/16	1/20
Domain of computation			
(fine)	$9\times2\times2$	$12\times2\times2$	$9\times1{\cdot}8\times1{\cdot}8$
(coarse)	$9\times4\times4$	$12\times4\times4$	$9\times3{\cdot}6\times3{\cdot}6$
Number of cells used	9×10^4	26×10^4	30×10^4
Reynolds number	10^3	10^3	10^3
Time increment	1/120	1/160	1/200
Time steps for acceleration	600	800	1000
	($T=5$)	($T=5$)	($T=5$)
CPU time ($T=20$) (TITAN-II)	30 h	100 h	150 h

Length and time are made dimensionless with respect to the diameter of a sphere and the uniform velocity.

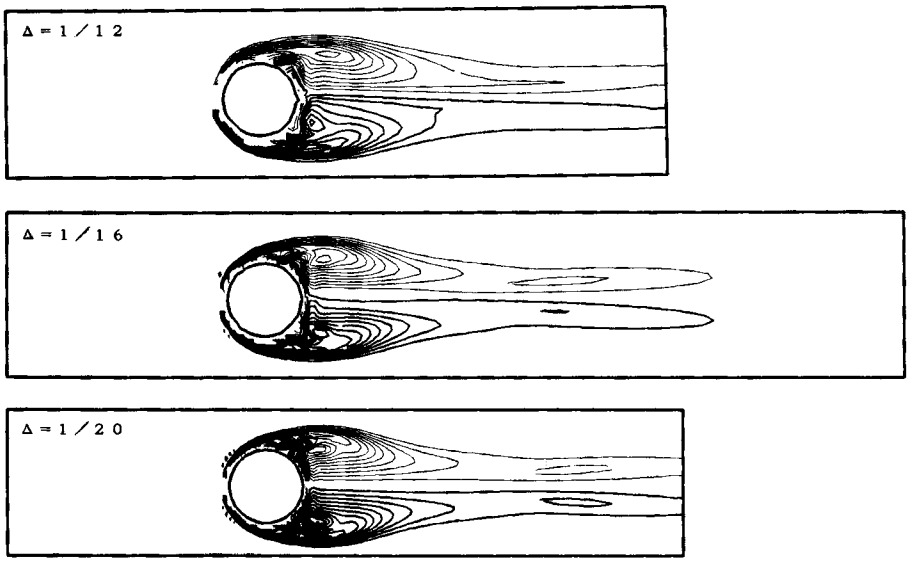

Figure 12. Comparison of vorticity field at $T=10$

5.2. *Numerical test*

The effect of the difference in grid spacing is illustrated in the contour map of spanwise vorticity (ω_y) on the horizontal centreplane in Figure 12. The differences among the three cases are mostly noted in the vicinity of the surface of the sphere where the strength of vorticity is largest.

The comparison of pressure distribution is made in Figure 13. The reduction in circumferential variation on the forepart of the sphere is assumed to be attributable to the smaller grid spacing, though it could be due to the three-dimensional structure of the flow on the afterpart.

The drag coefficient is calculated by integrating the pressure distribution on the sphere. The value obtained varies from 0·45 to 0·49, while the experimental value in the textbook by

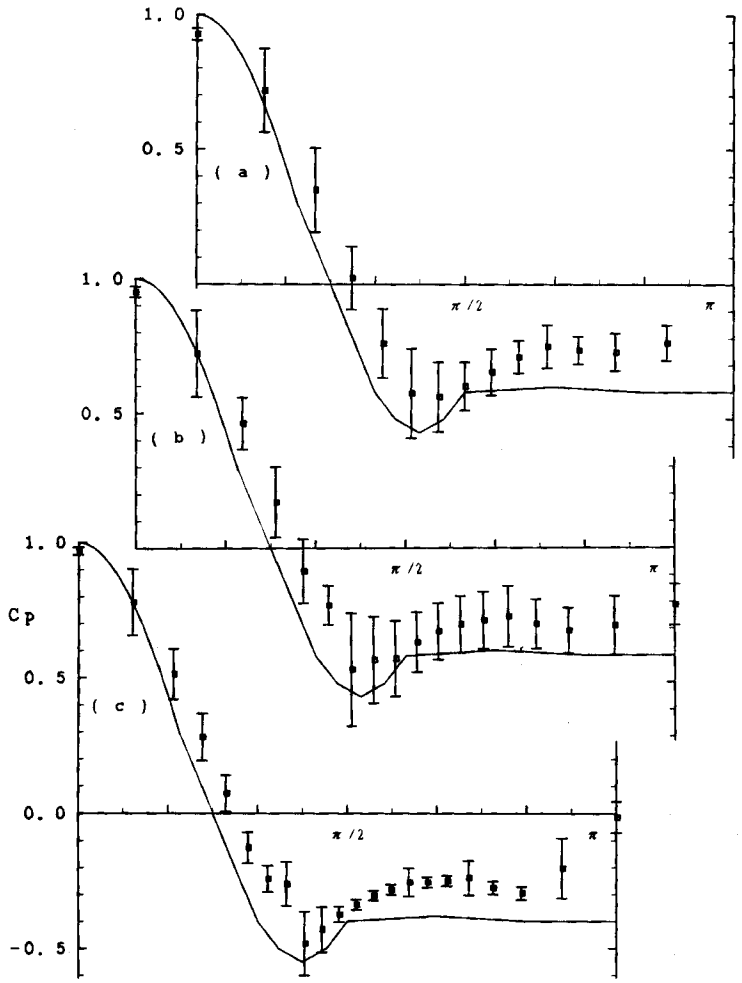

Figure 13. Pressure distribution on sphere at $T=10$: (a) $\Delta=1/12$; (b) $\Delta=1/16$; (c) $\Delta=1/20$; vertical bar indicates circumferential variation; solid curve is from experiment by Schlichting[13]

Hoerner[12] is 0·47 when the Reynolds number is between 10^3 and 4×10^5. The agreement is better than expected from the pressure distribution in Figure 13.

The degree of accuracy attained by the present method with the tested grid spacing is not very satisfactory. Therefore the present method should be applied with clear understanding of this inherent property, although the degree of accuracy is undoubtedly raised by decreasing the grid spacing.

The pressure contour map in the fine grid region is compared with that of the overall region in Figure 14. It is noted that the flow is continuously connected at the interface between the fine and coarse grid regions. The slight difference in contours in the inner region is due to the fact that only half the pressure points are used for the drawing within the inner region of the overall case in Figure 14.

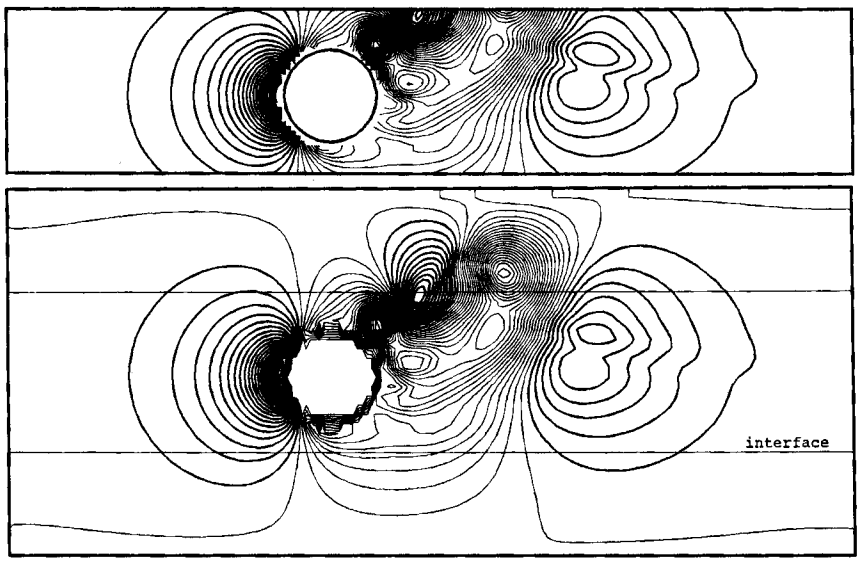

Figure 14. Pressure contour maps on x–y centreplane in fine grid region (top) and in whole domain (bottom), $\Delta = 1/20$, $T = 20$; contour interval 0·02; positive pressure drawn in bold lines

5.3. *Simulated flow*

We still do not have a comprehensive explanation of the separating flow past a sphere. Previous works by Taneda[10] and Achenbach[11] suggest that periodic vortex shedding, as in the case of flow past a circular cylinder, takes place and that an asymmetric structure may play an important role. However, the principal mechanism of vortex shedding, which corresponds to the Karman vortices from a circular cylinder, is not well elucidated owing to the complexity of the flow.

Even at this low Reynolds number of 1000, vortices with wide-ranging wavelength interact with each other and constitute the separating flow past a sphere. It is obvious that the grid spacing employed in this study can resolve only large-scale motions. However, the principal structure and mechanism may be well simulated. The constant spacing of the present method gives the advantage that the motions far behind the sphere can be resolved with the same degree of accuracy as in the near field.

The simulated results for case (b) with the spacing of 1/16 are shown in the form of vorticity contour maps in Figures 15–20 and Plate 1. After time level $T = 20$ the vortex-shedding motion is observed to be in a steady state. Figures 15–18 show the periodic elongation of the axisymmetric vortex ring of spanwise vorticity and the associated shedding of vortex tubes of streamwise vorticity. Since the period of vortex shedding is approximately 4·0, the Strouhal number is about 0·25, which is within the range observed in experiments.[10]

Although the results obtained are still limited and the structure is very complicated as expected, we can derive an understanding of the principal mechanism of vortex shedding from a sphere. Firstly, the separated shear flow forms a vortex ring of spanwise vorticity. Secondly, it is asymmetrically deformed and causes secondary vortices, mostly inside the vortex ring. The secondary vortices are entrained on the process of generating longitudinal vortex tubes, mostly of streamwise vorticity. When the vortex ring is elongated, it conceives and bring up longitudinal

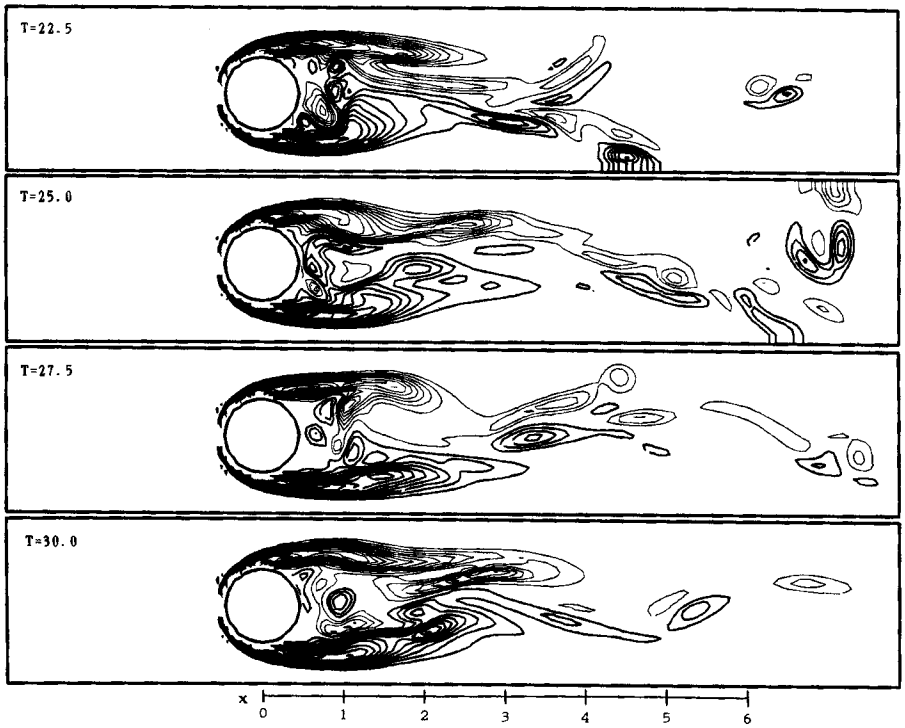

Figure 15. Time sequential development of ω_z on horizontal centreplane, $\Delta = 1/16$; contour interval 0·5; vorticity of anticlockwise rotation drawn in bold lines

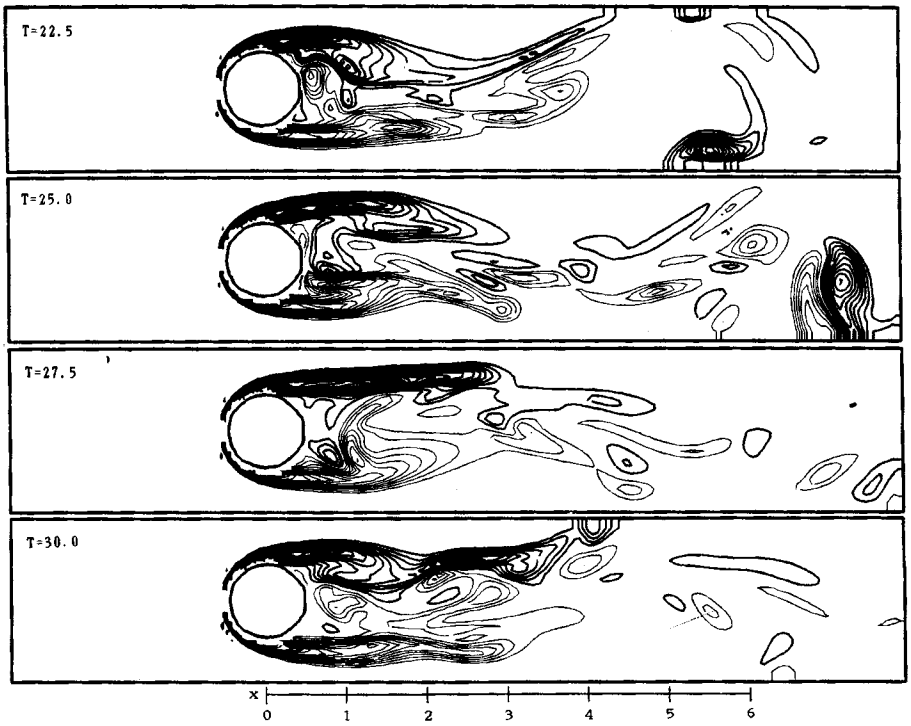

Figure 16. Same as Figure 15 but for ω_y on vertical centreplane; contour interval 0·5; vorticity of clockwise rotation drawn in bold lines

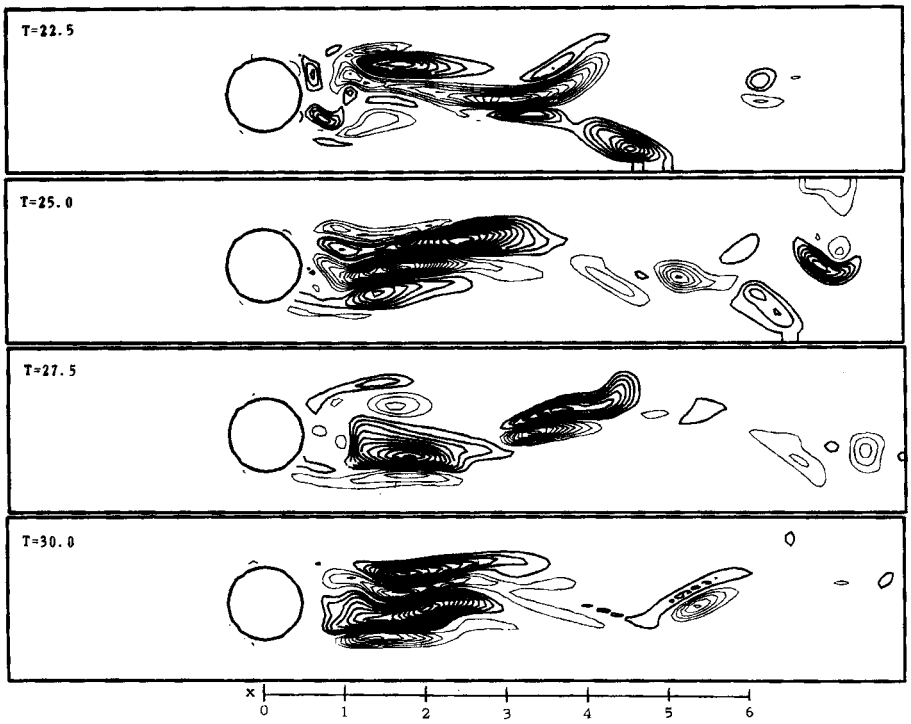

Figure 17. Time sequential development of ω_x on horizontal centreplane at same instances as Figures 15 and 16; contour interval 0·5; vorticity of anticlockwise rotation observed from upstream drawn in bold lines

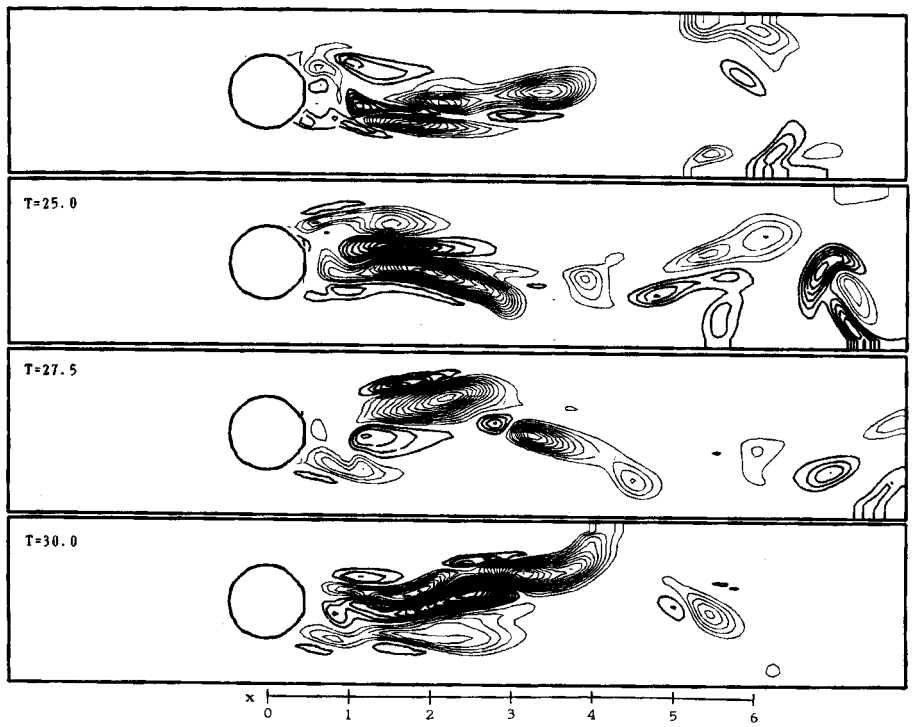

Figure 18. Same as Figure 17 but on vertical centreplane

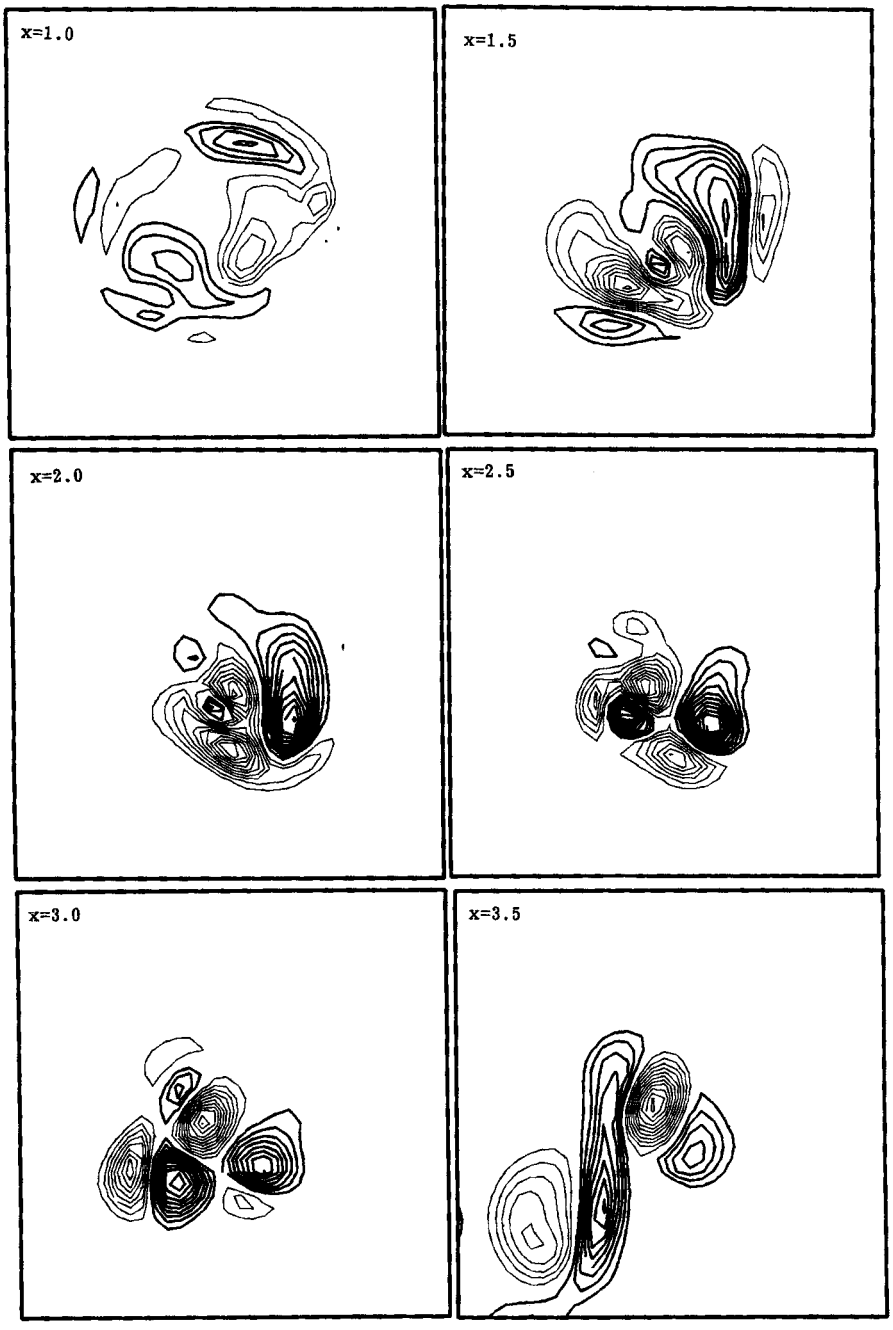

Figure 19. Contours of (a) ω_x and (b) ω_r on various cross-sections at $T=22{\cdot}5$, $\Delta=1/16$; contour interval 0·5; sense of rotation for ω_x same as Figures 15–17

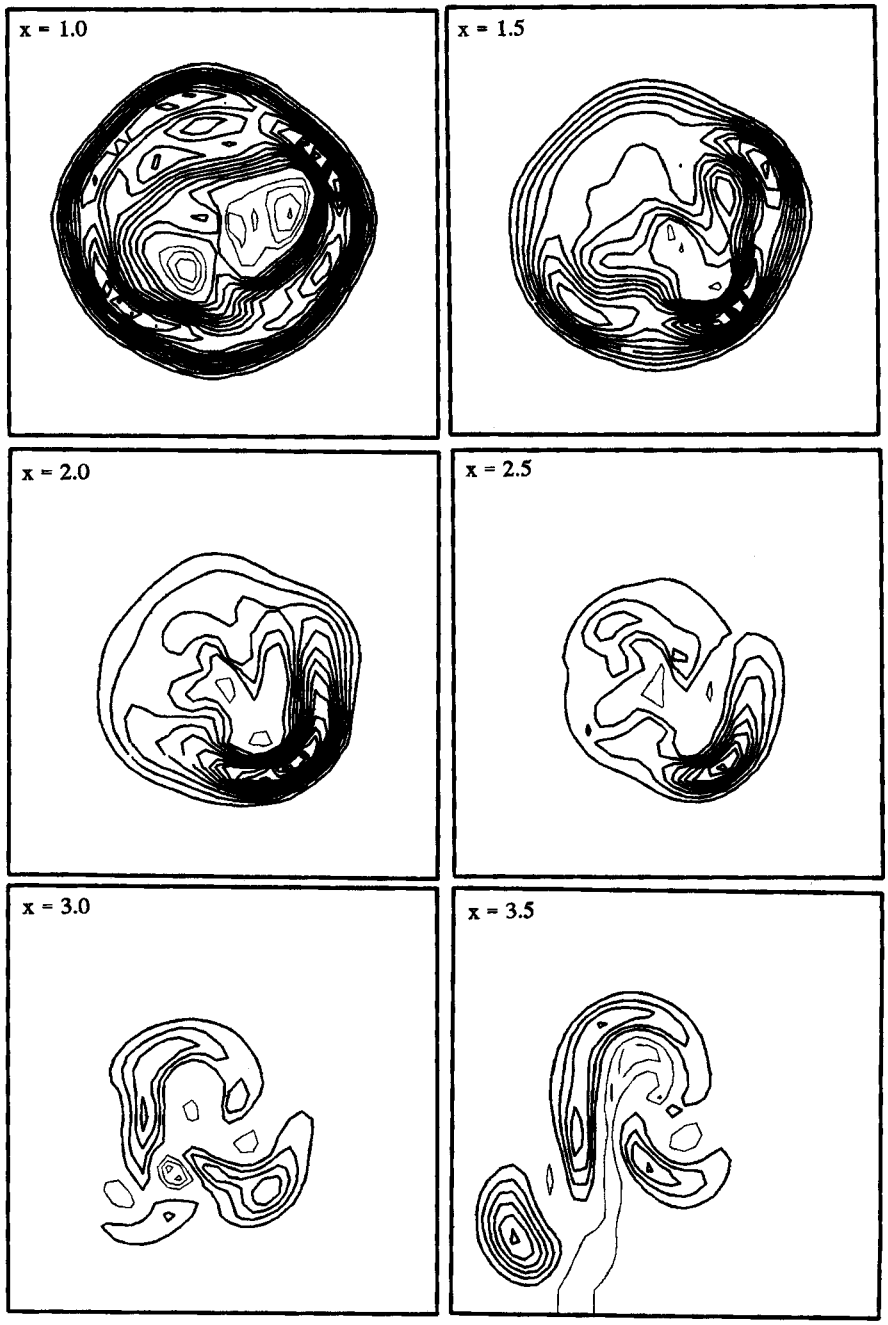

(b) T = 22.5, ω_r

Figure 19. (Continued)

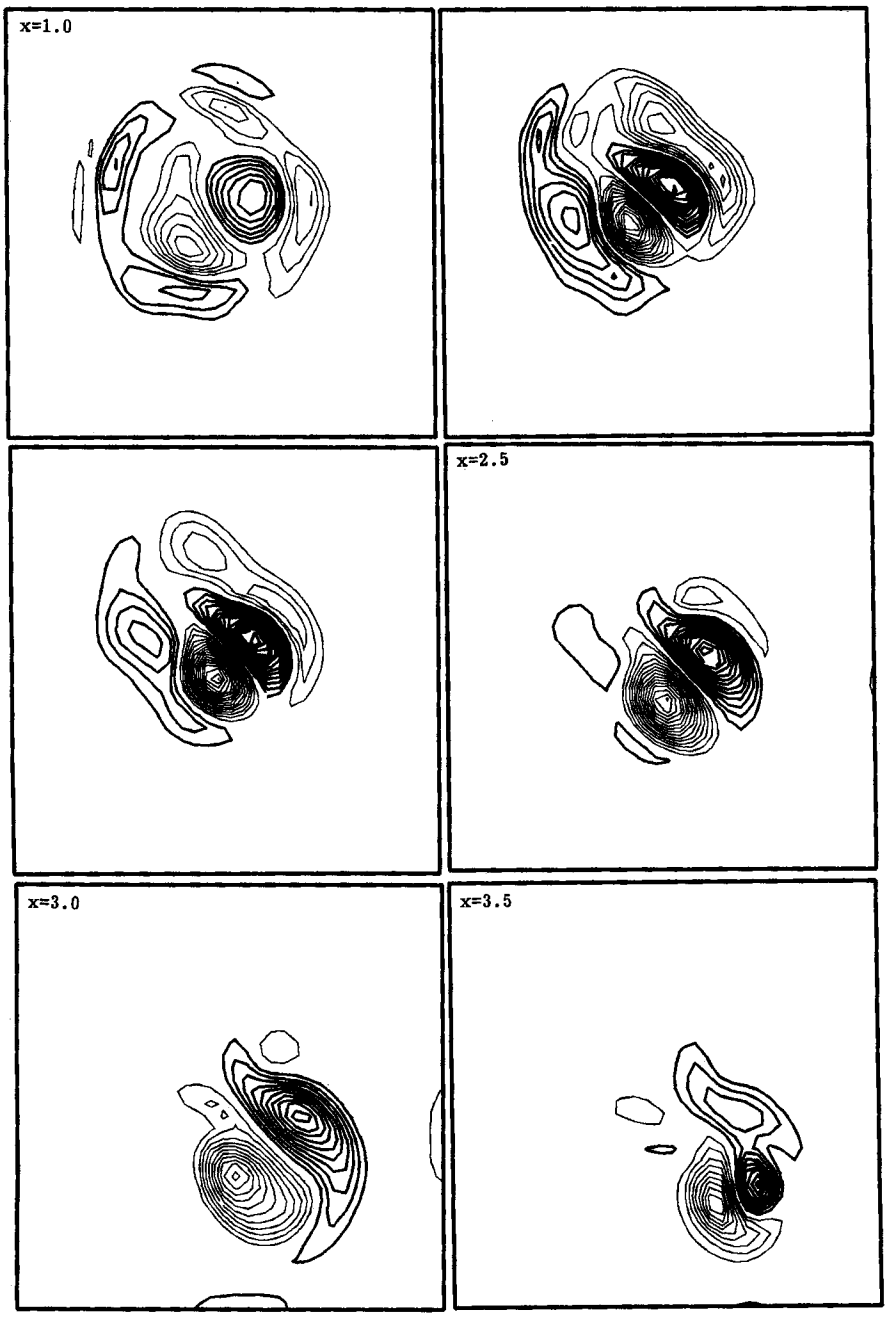

(a) T = 25.0, ω_x

Figure 20. Same as Figure 19 but at $T=25{\cdot}0$

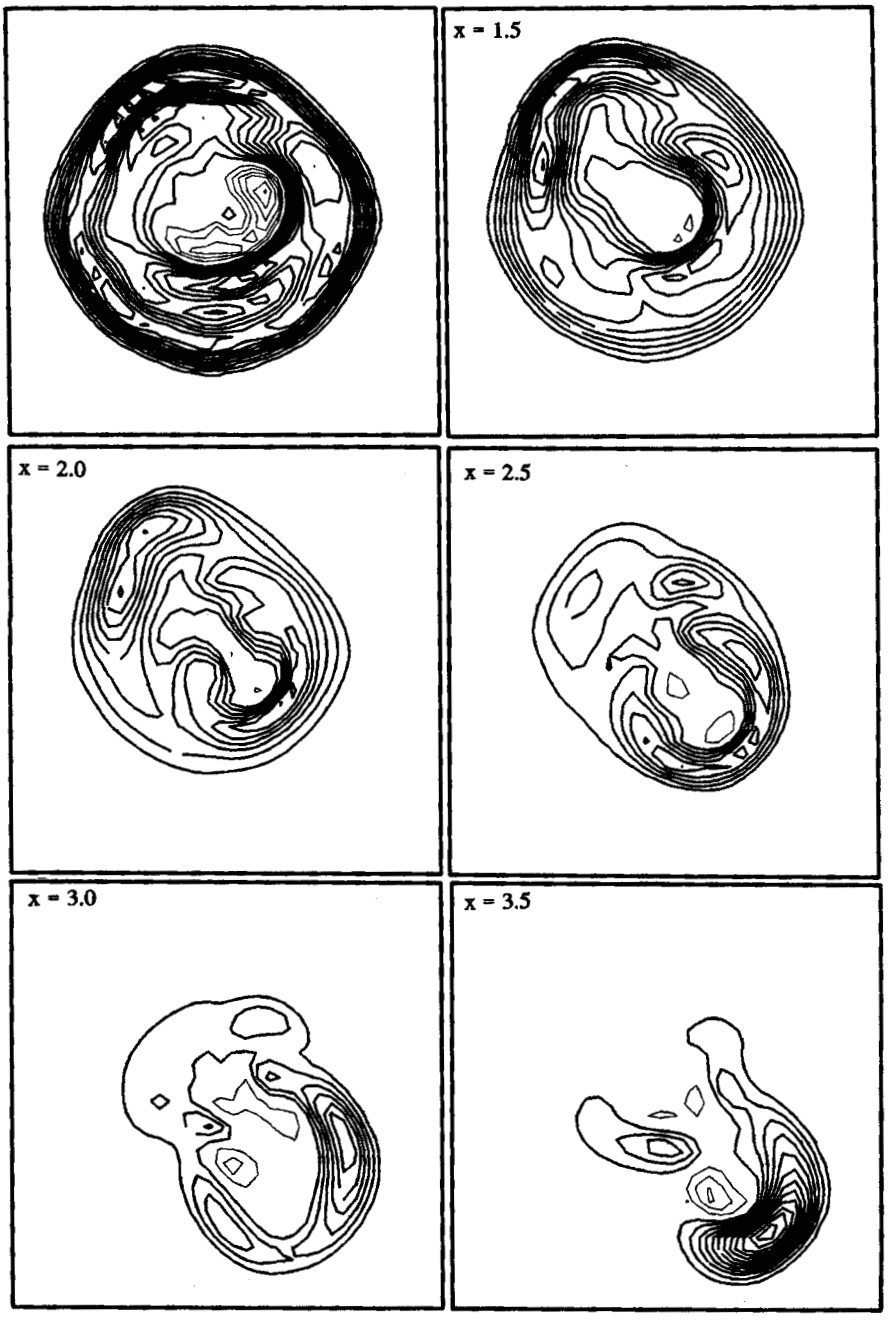

(b) T = 25.0, ω_r

Figure 20. (Continued)

vortex tubes inside the ring and is shortened when the longitudianl vortex tubes are shed behind. This is repeated periodically.

The cross-sections of the vorticity contours are shown in Figures 19, 20 and Plate 1 for three time levels in Figures 15–18, in which the origin of the co-ordinates is at the centre of the sphere. Assuming a cylindrical co-ordinate system with an axis passing through the sphere, the angular component of vorticity, ω_r, defined below is derived from ω_y and ω_z:

$$\omega_r = \omega_y \sin\psi - \omega_z \cos\psi. \tag{20}$$

Here ψ is taken from the y-axis towards the z-axis. It is noted that the ring vortex is mostly composed of spanwise vorticities ω_r and that the longitudinal vortex tube is mostly of streamwise vorticity ω_x, although all three components play an important role in the structure and mechanism of the separating flow past a sphere. One of the principal features of a longitudinal vortex tube is pairing with a counter-rotating tube. Therefore at any cross-section one or two pairs of counter-rotating vortex tubes are usually observed.

The equivorticity surfaces for the three components are drawn by computer graphic technology as shown in Plate 2, in which the equivorticity surfaces at the value of 0·5 are drawn. It is apparent that the vortex motion is of significant complexity. The above-described aspects of the simulated separating flow past a sphere are assumed to correspond to the result of flow visualization by Taneda[10] shown in Figure 21.

6. FLOW IN A BAY WITH AN ISLAND

6.1. Conditions of simulation

The water motions in the oceans are important because they influence the environment of the earth. However, up to now very little is known owing to the extremely large scale of the motion

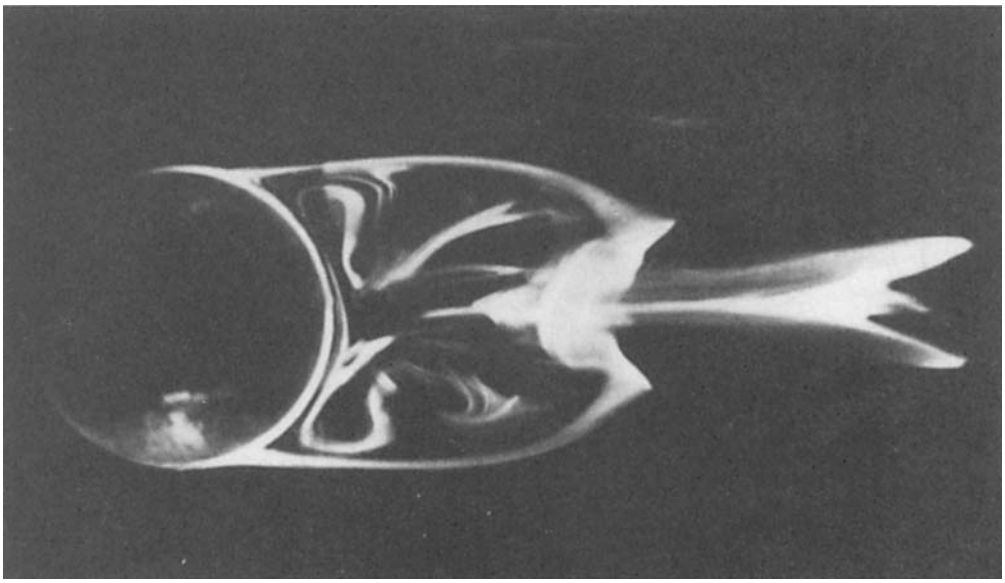

Figure 21. Visualized flow field at $Re = 300$ from Taneda[10]

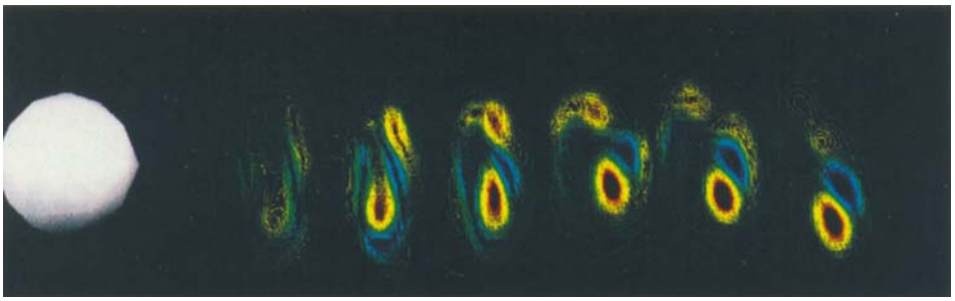

Plate 1. Contours of ω_x at $T=30$, $\Delta=1/16$; streamwise locations same as Figure 19

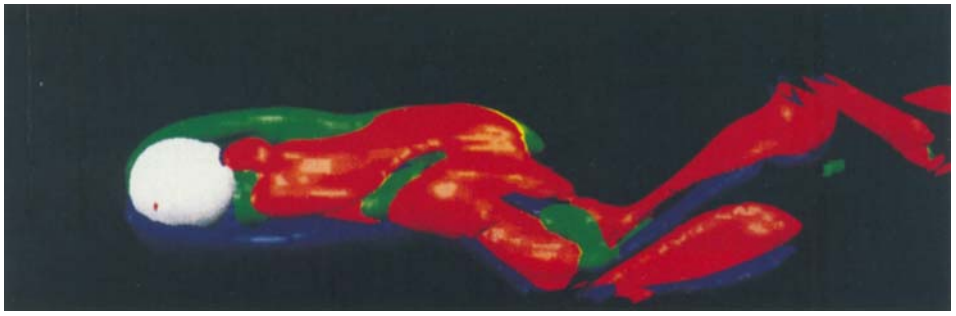

Plate 2. Computer graphic drawing of equivorticity surfaces for three components at 0·5, $T=30$, $\Delta=1/16$

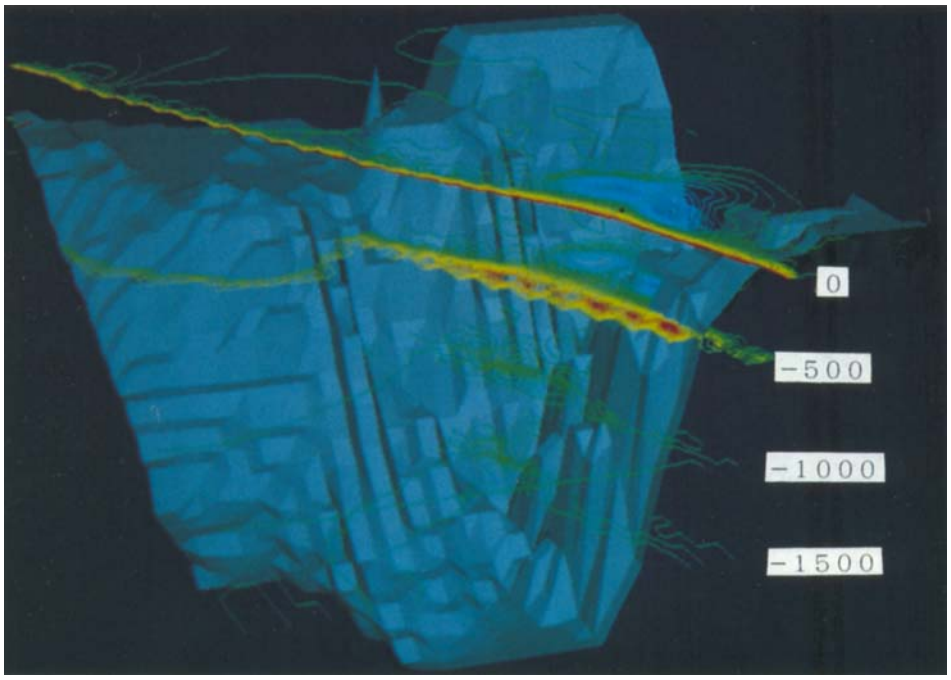

Plate 3. Contour map of horizontal velocity component u on horizontal planes at 0, 500, 1000 and 1500 m depth observed from south-east corner of computational domain; contour interval 0·02 ms^{-1}; positive values drawn in yellow to orange, negative values in blue; vertical co-ordinate 10 times magnified

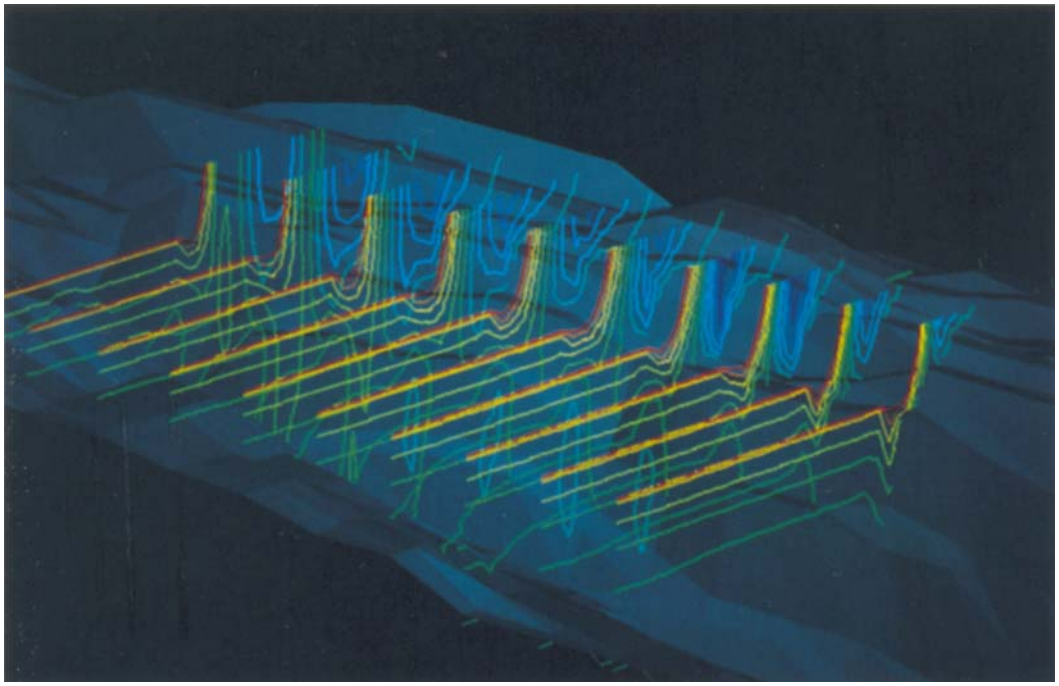

Plate 4. Contour map of horizontal velocity component u on vertical planes at intervals of 1·5km; orange lines indicate region of steady current; contour interval 0·06 ms^{-1}; x-co-ordinate 5 times magnified, z-co-ordinate 10 times

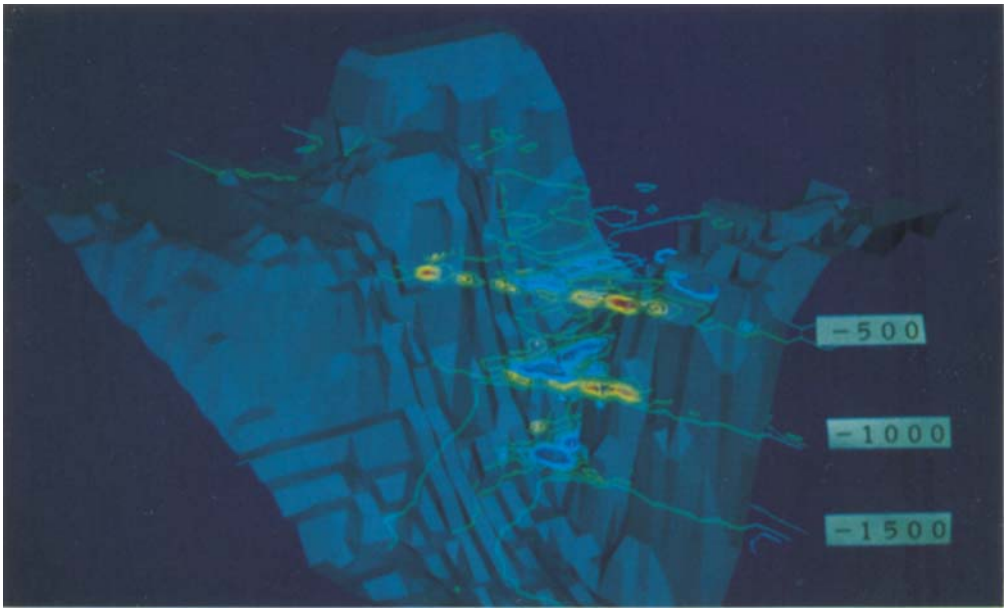

Plate 5. Contour map of vertical velocity component w on horizontal planes at 500, 1000 and 1500 m depth observed from south-east corner of computational domain; contour interval 0·008 ms^{-1}; positive (upward) values drawn in yellow to orange, negative (downward) values in blue; vertical co-ordinate 10 times magnified

and the high pressure beneath the ocean surface. Besides, the numerical simulations to which a great deal of efforts has been devoted in the past decade do not yet achieve a satisfactory state of technology, partly owing to the limited number of grid points used and the gross postulations made. In most cases the vertical motions and the effects of seabed geometry are only treated very approximately. The present numerical method described in the preceding sections seems to have the potential to overcome some of the shortcomings of the previous methods because it can cope with the problem of body boundaries of arbitrary configuration.

The flow in Sagami Bay is chosen here for a test computation to illustrate the application of our method to oceanographical problems. Sagami Bay is located near Tokyo city and is between Izu and Boso peninsulas. The maximum depth is about 2000 m and it contains Ohshima island, another small island and some seamounts. The isobathic contours of the southern part of Sagami Bay for the computation are shown in Figure 22.

The horizontal length of the computational domain is 75 and 90 km in the east–west (x) and north–south (y) directions respectively. This water region is divided into about 60 000 rectangular cells. The two horizontal lengths are divided into 50 and 60 in the x- and y- directions respectively and the maximum depth into 20. It is assumed that a steady current (gulf stream) of 3·92 knots is present in the southern part of the computational domain. It is directed towards the north-east direction at an angle of 26·6° to the latitudinal line. The Reynolds number based on the unit length of 15 km is set at 10 000 and the computation is continued until the non-dimensional time based on the unit length and the velocity of the steady current reaches 30.

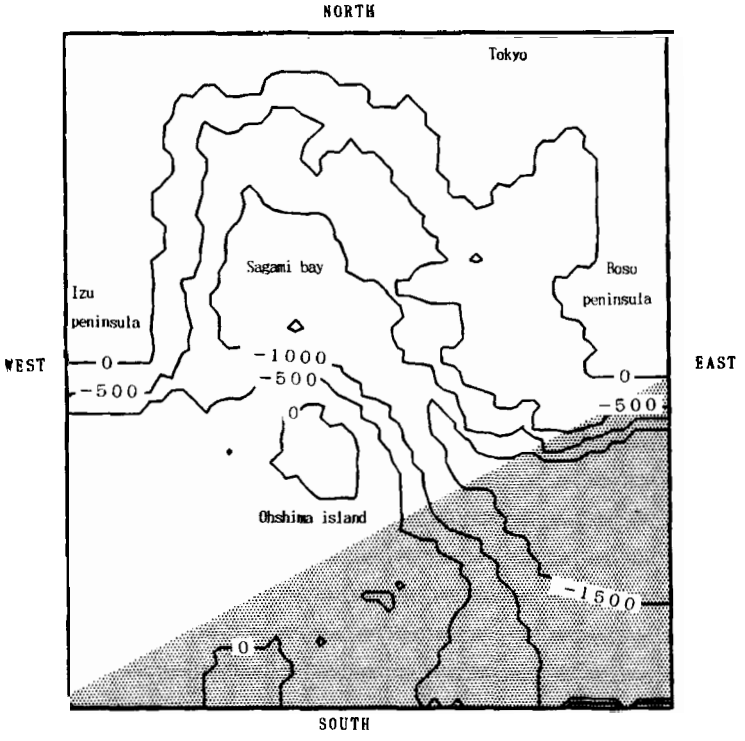

Figure 22. Isobathic contours of Sagami Bay (computational domain); interval 500 m; region of uniform current shown shaded

6.2. Simulation results

The simulation results at the non-dimensional time 30 are shown in Plates 3–5. The steady current induces reverse flow where the water depth is large as shown in Plates 3 and 4. The contour maps of the two velocity components indicate that the gulf current causes horizontal and vertical water motions in the 2000 m deep valley of Sagami Bay. Although the width of the gulf current is assumed to be 600 m, the vertical motion reaches down to the bottom of the valley.

It seems clear that fully three-dimensional fluid motions play an important role in the phenomena of oceans, although it is outside the scope of this paper to discuss the detailed structure and mechanism.

7. CONCLUDING REMARKS

A new simulation technique for flow about a body of complex geometry is developed within the framework of rectangular grid systems. The degree of accuracy is tested by simulation of the flow past a sphere, and the effectiveness of the method for ocean-engineering problems is shown by simulation of the flow in a bay with an island. It is demonstrated that the complicated structure of vertex motions can be elucidated by this method and that its robustness is rather high, although the degree of accuracy is evidently inferior to that of methods using boundary-fitted curvilinear grid systems in the close vicinity of a body surface. For problems with which the ordinary grid generation procedure presents serious difficulties and in which the delicate mechanism at the separation point does not give significant influences on the overall flow field, the present method will be useful.

Some interesting features of separating flow past a sphere are revealed by the present method and its usefulness is demonstrated by simulation of the flow in a bay of complex geometry. Although the grid spacing is coarse and the resultant degree of accuracy is not very good, it may be recognized that numerical simulations play an important role in elucidation of the structure and mechanism of complicated 3D flows.

ACKNOWLEDGEMENTS

This research is partly supported by a Grant-in-Aid for Cooperative Research from the Ministry of Education, Science and Culture and also by the LINEC group of shipbuilding companies in Japan. The authors are grateful for this support. They are also thankful to Ms. Onoda for her careful typing. The computer graphic drawings could not have been completed without the help of Mr. Miyachi of Kubota Computer Co., which is highly appreciated.

APPENDIX: NOMENCLATURE

A	defined by equation (8)
$\mathbf{a}$	source term
$\mathbf{b}$	source term
D	divergence
$\mathbf{F}$	external force
f	function
h	defined in Table V
I	operator defined by equation (13)
$\mathbf{M}$	numerical dissipation term

P	pressure
Re	Reynolds number
$\mathbf{S}$	matrix defined by equation (4)
T	non-dimensional time
t	time
Δt	time increment
u, v, w	velocity components in directions x, y and z respectively
x, y, z	co-ordinates
$\Delta x, \Delta y, \Delta z$	cell dimensions

Greek letters

α_4	parameter for differencing scheme
β	surface porosity
γ	volume porosity
Δ	spacing
ν_s	eddy viscosity coefficient
ω	relaxation factor or vorticity
ψ	angle in cylindrical co-ordinates

Superscripts

m	iterative level
n	time level

Subscripts

i	x-location of cell
j	y-location of cell
k	z-location of cell

REFERENCES

1. H. Miyata and T. Inui, *Nonlinear Ship Waves, Applied Mechanics, Vol. 24*, Academic, New York, 1984, pp. 215–288.
2. H. Miyata and S. Nishimura, 'Finite difference simulation of nonlinear ship waves', *J. Fluid Mech.*, **157**, 327–357 (1985).
3. J. E. Welch, F. H. Harlow, J. P. Shannon and B. J. Daly, 'The MAC method', *Los Alamos Scientific Laboratory Rep. LA-3425*, 1966.
4. C. W. Hirt, B. D. Nichols and N. C. Romeo, 'SOLA-A numerical solution algorithm for transient fluid flows', *Los Alamos Scientific Laboratory Rep. LA-5852*, 1975.
5. H. Miyata, S. Nishimura and A. Masuko, 'Finite difference simulation of nonlinear waves generated by ships of arbitrary three-dimensional configuration', *J. Comput. Phys.*, **60**, 391–436 (1985).
6. H. Miyata, T. Sato and N. Baba, 'Difference solution of a viscous flow with free-surface wave about an advancing ship', *J. Comput. Phys.*, **72**, 393–421 (1987).
7. H. Miyata and T. Kawano, 'Numerical simulation of the pseudo-physical transition to a turbulent flow on a suddenly decelerated flat-plate with and without riblets', *J. Soc. Naval Architect. Jpn.*, **165**, 17–28 (1989).
8. H. Miyata, 'Finite-difference simulation of breaking waves', *J. Comput. Phys.*, **65**, 179–214 (1986).
9. M. M. Rai, 'A conservative treatment of zonal boundaries for Euler equation calculations', *J. Comput. Phys.*, **62**, 472–503 (1986).
10. S. Taneda, *Fluid Dynamic Study by Photographic Image*, Asakura Shoten, Tokyo, 1988, pp. 38–39 (in Japanese).
11. E. Achenbach, 'Vortex shedding from spheres', *J. Fluid Mech.*, **62**, 209–221 (1974).
12. S. H. Hoerner, *Fluid Dynamic Drag*, Hoerner Fluid Dynamics, Brick Town, N.J., 1958, pp. 3–8.
13. H. Schlichting, *Boundary-layer Thoery*, McGraw-Hill, New York, 1979, p. 21.